# Soft, thin skin-mounted power management systems and their use in wireless thermography

Jung Woo Lee[a,b,1], Renxiao Xu[c,d,e,f,1], Seungmin Lee[a,1], Kyung-In Jang[a], Yichen Yang[a], Anthony Banks[a], Ki Jun Yu[a], Jeonghyun Kim[a,b], Sheng Xu[g], Siyi Ma[a], Sung Woo Jang[a,h], Phillip Won[a], Yuhang Li[i], Bong Hoon Kim[a], Jo Young Choe[a], Soojeong Huh[a,j], Yong Ho Kwon[a], Yonggang Huang[c,d,e,f,2], Ungyu Paik[b,2], and John A. Rogers[a,2]

[a]Department of Materials Science and Engineering, Frederick Seitz Materials Research Laboratory, University of Illinois at Urbana-Champaign, Urbana, IL 61801; [b]Department of Energy Engineering, Hanyang University, Seoul, 133-791, Republic of Korea; [c]Department of Mechanical Engineering, Northwestern University, Evanston, IL 60208; [d]Department of Civil and Environmental Engineering, Northwestern University, Evanston, IL 60208; [e]Department of Materials Science and Engineering, Northwestern University, Evanston, IL 60208; [f]Skin Disease Research Center, Northwestern University, Evanston, IL 60208; [g]Department of NanoEngineering, University of California, San Diego, La Jolla, CA 92093; [h]Department of Chemical and Biomolecular Engineering (BK21 Program), Korea Advanced Institute of Science and Technology, Daejeon, 305-701, Republic of Korea; [i]The Solid Mechanics Research Center, Beihang University (BUAA), Beijing 100191, China; and [j]Samsung Display Co. Display Research & Development Center, Yongin-City, Gyeongki-Do 446-711, Republic of Korea

Contributed by John A. Rogers, April 17, 2016 (sent for review February 25, 2016; reviewed by Ali Javey and Zhigang Suo)

**Power supply represents a critical challenge in the development of body-integrated electronic technologies. Although recent research establishes an impressive variety of options in energy storage (batteries and supercapacitors) and generation (triboelectric, piezoelectric, thermoelectric, and photovoltaic devices), the modest electrical performance and/or the absence of soft, biocompatible mechanical properties limit their practical use. The results presented here form the basis of soft, skin-compatible means for efficient photovoltaic generation and high-capacity storage of electrical power using dual-junction, compound semiconductor solar cells and chip-scale, rechargeable lithium-ion batteries, respectively. Miniaturized components, deformable interconnects, optimized array layouts, and dual-composition elastomer substrates, superstrates, and encapsulation layers represent key features. Systematic studies of the materials and mechanics identify optimized designs, including unusual configurations that exploit a folded, multilayer construct to improve the functional density without adversely affecting the soft, stretchable characteristics. System-level examples exploit such technologies in fully wireless sensors for precision skin thermography, with capabilities in continuous data logging and local processing, validated through demonstrations on volunteer subjects in various realistic scenarios.**

solid-state lithium-ion battery | multijunction solar cell | stretchable electronics | energy management | wearable technology

Recent ideas in materials science and mechanical engineering establish strategies for integrating functionality enabled by hard forms of electronics with compliant interconnects and soft packages to yield hybrid systems that offer low-modulus, elastic responses to large strain deformations (1–4). Such stretchable characteristics are qualitatively different from those afforded by simple mechanical bendability; the consequences are important because such properties allow for intimate, long-lived interfaces with the human body, such as the skin (5, 6), heart (7), and the brain (8), and for development of unusual device designs that derive inspiration from biology (9, 10). Many impressive examples of the utility of these concepts have emerged over the last several years, particularly in the area of biomedical devices, where work in skin-mounted technologies is now moving from laboratory demonstrations to devices with proven utility in human clinical studies (11, 12) and even to recently launched commercial products (13). Although schemes in high-frequency or ultrahigh-frequency wireless power transfer satisfy requirements in many important contexts (14, 15), opportunities remain for approaches in local generation and/or storage of power in ways that retain overall stretchable characteristics at the system level. Reported approaches to the former involve harvesting based on piezoelectric (16, 17), triboelectric (18), and thermoelectric (19) effects; the latter includes batteries (20–22) and supercapacitors (23, 24) enabled by various unusual materials. Complete power management systems that offer both types of functionality, in an actively coordinated fashion and with robust, high-performance operation, represent an important goal. This paper presents results that enable such operation in platforms that combine dual-junction compound semiconductor, millimeter-scale solar cells with bare die, chip-scale rechargeable lithium-ion batteries, and integrated circuits for power management. The integration schemes represent improvements on the types of liquid and ultrasoft elastomer strategies reported previously (1, 25), but in optimized, advanced architectures, including a folded, multilayer geometry that effectively combines the solar cells and batteries in a compact fashion without compromising the stretchable mechanics. System-level demonstrators involve thin, soft, compliant wireless systems configured

## Significance

Existing options for electrical power generation and storage in wearable electronics are incompatible with thin geometries, soft, stretchable mechanics, and lightweight construction needed for long-lived, intimate interfaces with the skin. Here we demonstrate concepts that allow the integration of collections of thin, millimeter-scale solid-state batteries and multijunction solar cells into electrically interconnected arrays that simultaneously provide high-performance operation and soft, biocompatible mechanics at the system level. Examples in photovoltaic energy harvesting, storage, and overall power management illustrate some of the functional options with such platforms. Thin, wearable wireless sensors for skin thermography with capabilities in data logging demonstrate the combined use of components for energy storage, power management, digital memory, physiological monitoring, and wireless, near-field communications in an integrated, stretchable device architecture with the ability to establish robust, nonirritating measurement interfaces directly to the skin.

Author contributions: J.W.L., Y.H., U.P., and J.A.R. designed research; J.W.L., R.X., S.L., K.-I.J., Y.Y., A.B., S.X., S.M., S.W.J., P.W., B.H.K., J.Y.C., S.H., and Y.H.K. performed research; J.W.L. and R.X. contributed new reagents/analytic tools; J.W.L., R.X., S.L., K.-I.J., K.J.Y., J.K., Y.L., Y.H., U.P., and J.A.R. analyzed data; and J.W.L., R.X., Y.H., U.P., and J.A.R. wrote the paper.

Reviewers: A.J., University of California, Berkeley; and Z.S., Harvard University.

The authors declare no conflict of interest.

Freely available online through the PNAS open access option.

[1]J.W.L., R.X., and S.L. contributed equally to this work.

[2]To whom correspondence may be addressed. Email: y-huang@northwestern.edu, upaik@hanyang.ac.kr, or jrogers@illinois.edu.

This article contains supporting information online at www.pnas.org/lookup/suppl/doi:10.1073/pnas.1605720113/-/DCSupplemental.

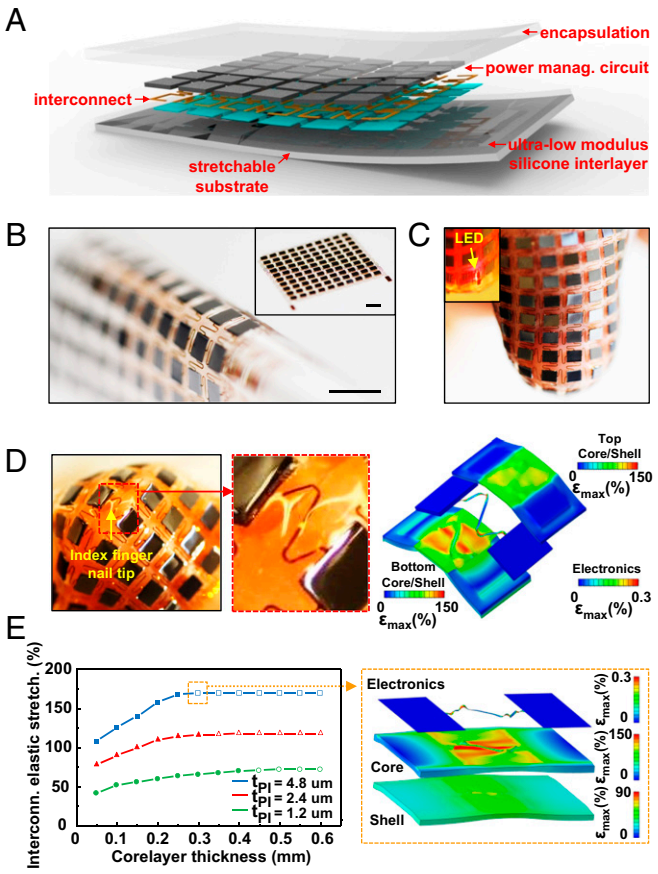


**Fig. 1.** Schematic illustration, 3D-FEA results, and images of thin, soft power supply systems that incorporate arrays of miniaturized device components joined by stretchable interconnect networks and contained in two-component elastomeric matrices. (*A*) Exploded-view illustration of the overall architecture of a system that includes a 6 × 6 square array of components. (*B*) Optical image of a device that includes a 10 × 10 array of chip-scale batteries bent around a cylindrical tube with a radius of 2.5 mm. (*Inset*) Image of the device in planar geometry. (Scale bars, 5 mm.) (*C*) A photo of the device shown in *B* wrapped around an index finger. (*Inset*) Activation of a red LED while in this deformed state. (*D*) Enlarged view of the components and interconnects at the tip of the finger (*Left*), and corresponding 3D-FEA results (*Right*), in exploded-view format for the top shell elastomer (10 μm) coated on the bottom with the core elastomer (0.3 mm) (*Top*), the device components and interconnect network (*Middle*), and the bottom shell elastomer (0.3 mm) coated with the core elastomer (0.3 mm) (*Bottom*). (*E*) Graph of the elastic stretchability as a function of thickness of the core elastomer for three different thicknesses of the polyimide layer in the interconnect network ($t_{PI}$) for the case of equal-biaxial tensile strain (*Left*). The hollow figures represent data points that exceed the computed limit of stretchability (*Right*) 3D-FEA result for the device components and interconnect network (*Top*), the soft core layer (*Middle*), and shell layer (*Bottom*) for the configuration illustrated by the dashed box in the graph (*Left*).

for autonomous skin thermography, with capabilities in data logging and local processing. These results, along with fundamental studies of the underlying issues in materials choices and mechanical designs, have the potential for widespread relevance in stretchable electronic technologies.

## Results and Discussion

Fig. 1*A* presents a schematic, exploded view illustration of an energy harvesting/storage/management system that exploits arrays of hard, miniaturized active components electrically interconnected and sealed within a two-component elastomer matrix. Here, optimized geometries in the serpentine wiring afford system-level, elastic stretchability with a low effective modulus; the elastomers provide strain isolation and environmental protection, in which an ultralow modulus core (modulus of ∼3 kPa, thickness of 300 μm; Silbione RT Gel 4717 A/B, Bluestar Silicones) allows freedom of motion of the serpentines and a shell (modulus of ∼60 kPa, thickness of 300 μm; Ecoflex 00–30, Smooth-on) encloses the entire system. The interconnects incorporate a trilayer stack of polyimide (PI) and copper, in the form PI(4.8 μm)/Cu (0.5 μm)/PI (4.8 μm) (*SI Appendix*, *note S1*). For the examples presented here, the components consist of either dual-junction (2J) compound semiconductor solar cells (∼32-μm total thickness, GaAs/InGaP, Microlink), chip-scale batteries (200 μm, lithium-ion Enerchip CBC005 and Enerchip CBC050, Cymbet) or some combination. A conductive alloy ($In_{97}Ag_3$, Indalloy 290, Indium Corporation) bonds these components to exposed pads in the interconnect network (*SI Appendix*, Fig. S1).

An energy storage system that includes a 10 × 10 array of chip-scale batteries appears in Fig. 1 *B–D*. Optical images show this module in a flat state (34 × 35 $mm^2$, Fig. 1*B*), bent around a cylindrical tube (radius of curvature 2.5 mm, Fig. 1*B*) and sharply wrapped around an index finger while providing power for the operation of a red light-emitting diode (636 nm, AlInGaP, $V_f$ = 2.0 V, LUMEX, Fig. 1*C*). In Fig. 1*D*, force applied by the tip of the finger (radius of curvature ∼4 mm) and the edge of the fingernail (radius of curvature ∼0.5 mm) induces large, local bending and stretching deformations. Even in such cases, the device exhibits an elastic response with little change in performance, consistent with 3D finite-element analysis (3D-FEA) that reveals maximum principal strains in the Cu that remain below the limit for plastic yielding (∼0.3%). These characteristics follow from the two-component elastomer configuration and optimized serpentine geometries, as described in detail in the following.

Comparative 3D-FEA study of systems with (Fig. 1*E* and *SI Appendix*, Figs. S2*A* and S3) and without (*SI Appendix*, Figs. S2*B* and S4*B*) the ultralow modulus core reveals its critical importance. Qualitatively, the core allows substantial out-of-plane bending and twisting of the serpentine interconnects, as they deform in response to externally applied load. This mechanism suppresses the occurrence of sharp bends and local wrinkling deformations, thereby reducing strain localization in the metal. Replacing the soft core with a more typical elastomer (i.e., modulus comparable to the shell) leads to stiffening of the surroundings in a manner that constrains freedom of deformation of the serpentines, resulting in the appearance of wrinkles with radii of curvature that are sufficiently small to induce strains (>∼0.3%) that lead to yielding of the metal. The strain/stress responses of the overall system also reflect these effects (*SI Appendix*, Fig. S5). Dynamic mechanical tensile testing and corresponding 3D-FEA modeling on the simplest unit (two solar cells joined by a serpentine interconnect) show quantitative agreement. For the core/shell system, the effective Young's modulus is only slightly (by ∼15%) higher than the value of an equivalent system without the active components or interconnects. Without the core, the corresponding moduli are different by a factor of 3, due to the strong coupling between the mechanics of the components and interconnects and the encapsulating elastomer. Such effects also influence the stretchability (*SI Appendix*, Fig. S6). A representative unit cell with core–shell design has elastic stretchability ∼39.2%, whereas that of an otherwise identical system without the core is only 9.7%. As additional characterization, *SI Appendix*, Fig. 5 *D* and *E* shows the strain/stress responses as a function of rate, from 5% strain per minute to 100% strain per minute. The results confirm some slight viscoelastic behavior, with an increase in modulus with frequency.

These favorable properties require, of course, a core region with sufficient thickness. Systematic study shows that for the particular materials and systems examined here (*SI Appendix*, Fig. S4*A*) thicknesses less than ∼200 μm begin gradually to compromise the mechanics. However, the effect of core thickness saturates such that, above a certain value (hollow figures; Fig. 1*E*), t_crit, the elastic stretchability is no longer sensitive to thickness. t_crit

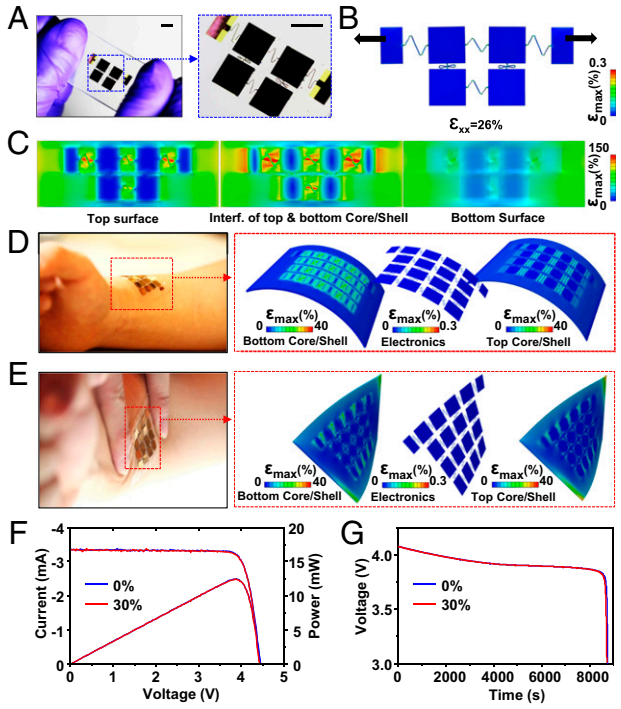


**Fig. 2.** Experimental and computational studies of the physics of buckling in an ultralow modulus silicone for strain isolation of assembled chips and interconnects. (*A*) Optical images of uniaxial stretching of a module that includes a 2 × 2 array of 2J solar cells. (Scale bars, 5 mm.) Three-dimensional FEA results of (*B*) the interconnect network and (*C*) top surface (to the left), the bottom surface (to the right) of the system, and the interface of top and bottom core/shell (middle). Optical images and 3D-FEA results of a corresponding 4 × 4 system laminated on the forearm in a (*D*) bent and (*E*) twisted configuration. Electrical performance of systems under biaxial stretching from 0 to 30% for the case of an (*F*) 2 × 2 array of 2J solar cells (current–voltage curves under AM 1.5 illumination) and a (*G*) 2 × 2 array of chip-scale batteries (charge–discharge curves).

depends most strongly on the materials and geometric parameters, particularly the cross-sectional dimensions, of the interconnects. Three-dimensional FEA indicates that as the interconnect thickness increases (and consequently their stiffness), t_crit decreases. A likely explanation is that deformations of stiff interconnects are dominated by their intrinsic structure, with reduced dependence on the properties of the surrounding material. Computational analysis aids in selection of optimized serpentine geometries and PI thicknesses. A key finding is that longer serpentines in patterns with increased complexity (e.g., geometrically self-similar, or fractal designs) do not necessarily provide improved elastic stretchability, as evidenced by the comparisons in *SI Appendix*, Figs. S6 and S7. Here, complex shapes tend to involve strain concentrations that counterbalance the benefits expected from their increased contour lengths, thereby preventing them from reaching their full capacity in stretchability. This observation is qualitatively different from those in systems that use microfluidic core regions.

Results in Fig. 1*E* and *SI Appendix*, Fig. S8 indicate that moderately thick PI layers can promote elastic stretchability whereas excessively thick PI layers have the opposite effect. The PI thickness in the former regime diminishes the occurrence of local wrinkling deformations, thereby preventing strain localization in the metal. Instead, a global buckling mode results (26), such that the interconnects can achieve nearly their full extension without failure. For the latter case, the large thickness in the PI leads to a large bending stiffness that prevents out-of-plane buckling. Here, in-plane bending dominates, with reduced stretchability. In other words, this nonmonotonic dependence on PI thickness arises from a gradual transition of the deformation mode from one defined by local wrinkling (in the limit of small thickness) to global buckling (moderate thickness) to in-plane bending (large thickness) with increasing thickness.

These systematic investigations of material configurations and serpentine designs allow optimized construction at the module level. Choices in serial and parallel connection schemes in the arrays of solar cells and batteries afford significant versatility in the selection of output currents and voltages (*SI Appendix*, Figs. S9 and S10). In addition, the serpentine interconnects and core/shell designs allow low effective modulus and high stretchability even at large areal coverages of active components. *SI Appendix*, Figs. S11 and S12 summarize studies of reversible mechanical deformation of solar and battery modules for 30% equal-biaxial stretching. Here, local regions of the elastomers reach strains >100%, while the maximum principal strains in the metal interconnects remain below the yield point (0.3%). This strain isolation and the full recovery of serpentine geometries upon release of the load leads to completely reversible, elastic deformation across all components of the systems. Three-dimensional FEA modeling indicates that both the solar and battery modules can undergo total biaxial elongation up to ∼55% and ∼45%, respectively, before fracture in the interconnects, almost twice as stretchable as human skin (*SI Appendix*, Fig. S13) (5). In all cases, deformations of devices with the core/shell design show minimized constraints in motion of the components or the interconnect network compared with designs without the core, as demonstrated by the uniform distributions of overall strain in a supporting substrate (*SI Appendix*, Fig. S14). Addition of an encapsulating layer reduces the elastic stretchability only slightly (from 39.7% to 39.2%) as shown in *SI Appendix*, Figs. S3, S15, and S16.

Both areal coverage and stretchability can be further enhanced by use of a strategy that involves application of prestrain to the elastomer base immediately before integration with the components and interconnects (27). *SI Appendix*, Fig. S17*A* presents images from experiments and 3D-FEA modeling with a test structure that consists of four unit cells at the center of a larger module, corresponding to configurations immediately after release of the prestrain and at the limit of elastic stretchability under biaxial tensile loading. For the solar cell array, prestrains of up to ∼10% are possible; beyond this value, the interconnects begin to come into close physical proximity, approaching contact, although even higher levels of prestrain are possible without electrical failure. At 10% prestrain, the areal coverage of functional components increases from ∼60% to ∼73%, and the elastic stretchability from ∼39% to ∼53%, and the total stretchability from ∼55% to ∼71%.

These mechanical characteristics are important not only in uniaxial or biaxial stretching, but also in bending, twisting, and other more complex deformations (Fig. 2 *A*–*C* and *SI Appendix*, Fig. S17*B*). The elastic limits are not the same for these different modes. For example, the device described above (without prestrain) exhibits elastic stretchability of 26% and 36% along the x- and y directions, respectively. These values are somewhat lower than those for the case of biaxial stretching, simply due to Poisson compression of the interconnects along the direction normal to the loading direction, ultimately into self-contact at the limits. Experiments show that a 4 × 4 solar module can wrap the human wrist (Fig. 2*D*), twist with ∼60° (Fig. 2*E*), and locally stretch or compress around fingers (*SI Appendix*, Fig. S17*C*). In all cases, the maximum strains in the 2J cells and the metal of the interconnects reach only ∼0.1%, much below the semiconductor fracture strains (∼1%) and metal yield strains (∼0.3%), and more than 2 orders smaller than the strains in the surrounding elastomers (∼20–40%).

The electrical properties of the interconnect networks remain invariant under such types of deformation, as supported by a lack of measurable change in the resistance for equal biaxial stretching up to 50% (*SI Appendix*, Fig. S18). Measurements of the

electroluminescence from solar modules and the output voltages of battery modules reveal stable operation at 30% biaxial strain as in *SI Appendix*, Figs. S19 and S20, respectively. The results in Fig. 2*F* indicate that a module consisting of a 2 × 2 array of 2J solar cells in half series/parallel connection (*SI Appendix*, Fig. S8) produces an open-circuit voltage and a short-circuit current of 4.4 V and 3.4 mA, respectively, under AM 1.5 illumination (91192, Oriel). The maximum power and fill factor are 12.5 mW and 0.84, respectively. The performance is unaffected by equal biaxial stretching to 30%. Cyclic deformation tests under uniaxial stretching to strains of 15% reveal no changes for 1,000 cycles (*SI Appendix*, Fig. S21*A*). Corresponding battery modules also show expected behaviors, as in Fig. 2*G* for an example that involves a 2 × 2 array of chip-scale batteries connected in parallel (*SI Appendix*, Fig. S9). The module produces ∼3.8 V at a discharge current of 100 μA (Gamry Reference 600, Gamry Instruments) over a period of 2 h in both undeformed and biaxially stretched (30%) states. The characteristics (measured at 500 μA) are invariant during 1,000 cycles of uniaxial stretching to 15% strain (*SI Appendix*, Fig. S21*B*).

The design approaches reported here offer considerable versatility in layout geometries and electrical output characteristics (*SI Appendix*, Fig. S22). As an example, a solar module that involves a 4 × 4 array of 2J solar cells all connected in series (*SI Appendix*, Fig. S9) produces open-circuit voltages and short-circuit currents of 33.1 V and −1.59 mA, respectively, with a maximum power of 43.0 mW (*SI Appendix*, Fig. S23*A*). Similarly, a 4 × 4 array of chip-scale batteries connected in parallel (*SI Appendix*, Figs. S9, S23*B*, and S24) exhibit an ∼4.5× increase in storage capacity compared with a 2 × 2 array. The discharge current is 500 μA (*SI Appendix*, Fig. S21*B*) and the maximum power reaches 77.3 mW for 20-mA output for ∼2 min. These power levels can satisfy practical requirements in several recently demonstrated types of stretchable skin-mounted electronic devices (1).

The soft mechanics of these systems not only affords options in mounting on the skin, but also in laminating onto one another, as an unusual form of electrical integration. As shown in *SI Appendix*, Figs. S25 and S26, a solar module can be flipped and laminated on top of a battery module, thereby establishing electrical contacts. The battery module can be charged in this way by placing the integrated pair in a lighted area. After charging, the solar module can be replaced by a light-emitting diode (LED) module, in a similar architecture, using the same approach. The output voltage of this battery module is sufficient to operate a blue LED (463 nm, InGaN, $V_f$ = 3.3 V, LUMEX) as a demonstration. The adhesive nature of the core material provides a robust mechanical joint, suitable even for operation under water (*SI Appendix*, Fig. S26*B* and Movie S1).

In addition to lamination, the extreme deformability of these systems allows their construction via folding to yield multilayer designs with reduced overall lateral dimensions (*SI Appendix*, Fig. S27 and Table S1*A*). Fig. 3*A* shows a photograph of a device that includes a small array of solar cells, batteries, and a power management circuit, designed for this purpose. This latter unit mediates the functions of the solar cells and batteries, and facilitates efficient power regulation of the overall system. Here, a set of fabrication steps similar to those described previously yields an assembled set of interconnected components on a shell elastomer (300-μm thickness) coated with a layer of the soft core material (300-μm thickness). Casting another layer of this core material (200-μm thickness) on top of the devices, partially curing this material, folding the entire structure, and then completing the curing process concludes the fabrication. Fig. 3*B* summarizes the strain distribution in the metal layer, obtained by FEA, at different steps in folding. Even the most severely deformed regions have strains that are considerably smaller than the yield strain of the copper (∼0.3%), as highlighted in the four subpanels. Fig. 3*C* shows a side view. Three-dimensional FEA results and experimental observation both suggest the cross-section of the folded region takes a

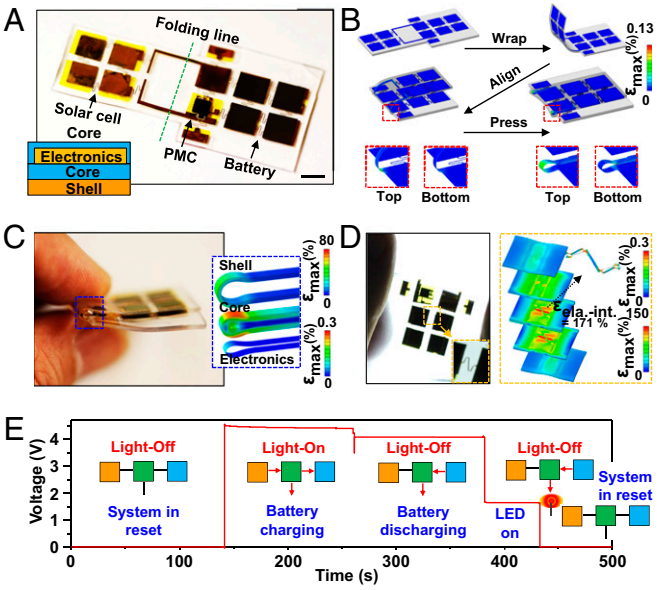


**Fig. 3.** Images, 3D-FEA results, and operational data for a solar cell and battery-integrated power control system realized by folding. (*A*) Image of an energy harvesting/storage/supply system that includes a 2 × 2 array of 2J solar cells, a 2 × 2 array of chip-scale batteries, and a power management chip in planar geometry, before folding. (*Inset*) A cross-sectional illustration of the key layers. (Scale bar, 5 mm.) (*B*) Three-dimensional FEA results of the system at various stages of the folding process. (*C*) Image of the folded device and exploded-view 3D-FEA results of the maximum strain distributions near the fold for the shell elastomer (top), the core elastomer (middle), and the interconnect structure (bottom). (*D*) Image and exploded-view 3D-FEA results under uniaxial stretching for the top shell, top core, electronics, center core, electronics, bottom core, and bottom shell layers, from top to bottom. (*E*) Graph of the output voltage of the system with/without light and operation of an LED. The schematic diagrams illustrate each component of the system with colored boxes (orange, solar cell; green, power management circuit; blue, battery) and the red arrows indicate the direction of power flow.

teardrop-, or tennis racket, shape, as is typical of folded elastomeric bands, but in a way that spontaneously fills with the soft core material (28). The core accommodates the most severe deformations, whereas the circuit layer undergoes almost pure bending, with minimal strain. This strain isolation effect can be quantitatively revealed by examining the distribution of strain in each layer. For instance, the maximum strains in the metal of the interconnects and the core material are ∼0.1% and ∼80%, respectively. *SI Appendix*, Fig. S28*A* shows images of the folded device collected by X-ray computed tomography. The solar cells and batteries stack on top of one another, and the serpentine interconnects overlap with good alignment. The mechanics of this configuration leads to a computed elastic interconnect stretchability of ∼170% unidirectionally (Fig. 3*D*). This value is almost the same as that for systems in a single-layer design (i.e., without folding), thereby establishing that the stretchable mechanics is not adversely affected by well-aligned folding into a bilayer geometry.

The electrical characteristics of the device appear in Fig. 3*E*, determined using the chronopotentiometry method (Gamry Reference 600, Gamry Instruments). The output voltage (potential difference between $V_{OUT}$ and $V_{GND}$) is 0 V before exposure to light (i.e., "light on"), due to operation of the power regulation unit (CBC910, Cymbet) in a "sleep" mode. The internal control logic deactivates the charge pump to minimize current consumption when the battery current is not needed. Light illumination increases this voltage to ∼4.4 V, by consequence of contribution from the solar cells (connected to $V_{DD}$ for positive supply and $V_{GND}$ for negative supply). Here, an internal field-effect transistor (FET) switch in

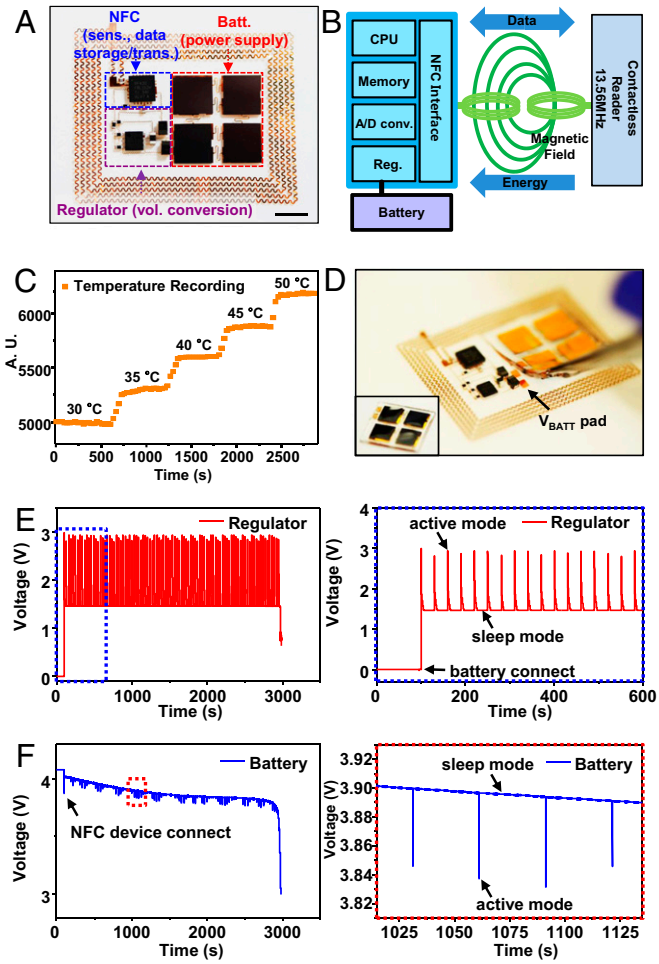


**Fig. 4.** Images, schematic illustration, and operational data of for a stretchable battery-integrated system capable of temperature logging and wireless data transmission. (*A*) Optical image of the system, with colored boxes and labels to identify the various subsystems, including the NFC electronics/sensor/data storage module, a 2 × 2 array of chip-scale batteries, and a power regulator. (Scale bar, 5 mm.) (*B*) Schematic diagram of overall system operation with data logging. (*C*) Data (arbitrary units) collected during exposure of the device to a stepwise increase in temperature. (*D*) Image of the system with releasable battery module. Voltage monitoring of the (*E*) regulator and (*F*) battery. Graphs (*Right*) provide detailed views that illustrate the active and sleep modes.

the regulator routes $V_{DD}$ to $V_{OUT}$ during normal operation when $V_{DD}$ (the output voltage of the solar cell) is above a set voltage (~2.5 V). At the same time, the solar cells also activate the charge pump for the purpose of charging the batteries at ~4.1 V. Upon removal of light (i.e., "light off"), $V_{DD}$ falls below the set voltage and the FET switches such that the output voltage (connected to $V_{BAT}$ for positive supply and $V_{GND}$ for negative supply) is equal to the battery voltage (here, ~4.06 V). When a red LED (SSL-LX5093IT, 635 nm, max $V_f$ = 2.5 V, LUMEX) connects to the device (i.e., "LED on"), the voltage drops to ~1.65 V for the operation of the LED [i.e., 1.65 V = ~4.06 ($V_{BATT}$) − ~2.41 (voltage associated with the LED)]. Finally, the output voltage returns to 0 V when the battery level falls below a separate set point (here, ~3 V) during external device operation. Here, the power management circuit shuts off the power supply to protect the battery (i.e., "system in reset"). All performance characteristics remain unchanged even during stretching (*SI Appendix*, Fig. S28*B*).

Integration of these concepts in stretchable power supply can be exploited in skin-mounted, wireless sensor systems. Demonstrations described here involve advanced near-field communication (NFC) technology for continuous logging of temperature and wireless data transfer. Fig. 4*A* presents an optical image of a device that consists of three different parts: an advanced NFC chip (RF430FRL152H, Texas Instruments) which includes a temperature sensor, a wireless (13.56 MHz) communication module, and onboard memory; a regulator that interfaces to the battery to control operation; and the battery itself. Integration uses the reversible lamination process described earlier, thereby allowing the battery to be removed for recharging and then reapplied for operation (as shown in Fig. 4*D* and *SI Appendix*, Fig. S29*A* and Table S1*B*). The system senses temperature and stores the resulting information in onboard memory at a rate of one event every 30 s. In between sensing and storing events, the operation reverts into a low-power sleep mode. When placed into proximity of an active NFC reader, the system automatically transmits these data to the reader, as shown in Fig. 4*B*. Fig. 4*C* presents a demonstration of data logging during a stepwise increase of temperature (*SI Appendix*, Fig. S30). The observed linear relationship establishes a calibration curve between the reading from the device and actual temperature (*SI Appendix*, Fig. S31). Fig. 4 *E* and *F* summarizes the output voltage from the built-in regulator inside the NFC chip and the corresponding

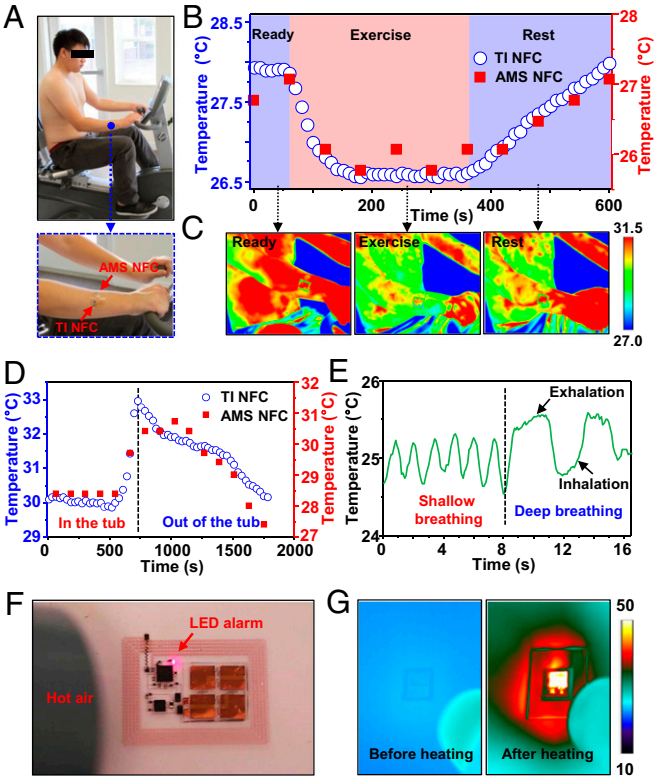


**Fig. 5.** Practical application examples of skin-mounted, stretchable systems capable of temperature logging and wireless data transmission. (*A*) Optical images of a device laminated onto the forearm of a subject during exercise on a stationary bike. (*B*) Temperature data recorded immediately before ("ready"), during ("exercise"), and immediately after ("rest") exercise on the bike, where the red squares correspond to temperature determined in an adjacent skin-mounted NFC device without a battery module (AMS NFC); the open circles correspond to the battery-integrated system (TI NFC). (*C*) IR images corresponding to each stage of the evaluation. (*D*) Graph of temperature response to breathing. (*E*) Graph of change in the temperature of skin on the forearm during immersion of the lower body in warm water. (*F*) Image of a device during application of hot air, to illustrate illumination of a red LED as an indicator of temperature values above a set threshold and (*G*) IR images before and after applying hot air.

changes in voltage from the 2 × 2 chip-scale battery module. A regulator (BD9120, ROHM Semiconductor) switches the output voltage of the battery to ∼1.5 V, to match the requirement of operation of the NFC chip, as long as battery voltage is between 2.7 and 4.5 V. With sleep/wake intervals of 30 s, the system can sense the temperature and store the data into the onboard memory of the NFC over a time of nearly 3,000 s, as shown in Fig. 4*F*. The *SI Appendix* presents embodiments that offer extended operation time (*SI Appendix*, Fig. S32 *A* and *B*) and wireless monitoring of battery voltage (*SI Appendix*, Fig. S32*C*).

Fig. 5 summarizes an example of extended use in a realistic scenario in which skin-mounted operation allows continuous monitoring of temperature during physical exercise. Here, the device laminates onto the forearm of a volunteer on a stationary bike; a separate, wirelessly powered NFC (SL13A, AMS) device (15) placed on an adjacent region of the arm collected data at a sampling rate of 1 point/1 min via NFC-equipped smartphone (Galaxy Note 4, Samsung) to provide a set of data as a control (Fig. 5*A*). The results appear in Fig. 5*B*, where the data show variations in temperature during "ready," "exercise," and "rest" stages, at a sampling rate of 1 point/10 s over 10 min. The skin temperature drops shortly after beginning the exercise, as a result of sweat gland activity and evaporation from the skin surface. During the rest, the temperature recovers to the original state, as expected based on homeostasis (29). The battery and wirelessly powered devices show similar responses. Data collected by an infrared (IR) camera (FLIR SC650) (Fig. 5*C*) represent an additional point of comparison. As an illustration of the waterproof nature of the systems, Fig. 5*D* presents results of an experiment in monitoring of skin temperature during bathing. Here, the volunteer immerses his body, with devices mounted on the skin, in warm water (∼43 °C) for 8 min. During this time, the temperature stabilizes to a constant value. As with observations of homeostasis associated with exercise, the temperature increases to 33 °C shortly after the subject moves out of the tub and then slowly returns to the initial value.

As additional example, at high sampling rates (10 points/1 s) it is possible to measure temperature variations associated with processes such as respiration (Fig. 5*E*). In a more advanced example, incorporating a red LED (625 nm, InGaAlP, Osram Opto Semiconductor) enables a visual indicator of excessively high (above 40 °C) or low (below 10 °C) temperatures during bathing, swimming, or other activities (Fig. 5 *F* and *G* and *SI Appendix*, Figs. S29*B* and S33, and Table S1*C*). Such functionality might be helpful in the prevention of hypothermia, hyperthermia, burns, or frostbite. Fig. 5*F* and Movie S2 show activation of the LED due to flow of hot air from a hair dryer onto the skin; here, the temperature of the skin exceeds 40 °C as visualized by the IR camera images in Fig. 5*G*. The system can be configured such that the LED also activates when the temperature decreases below a certain level by, for example, placing it in cold water or on ice (*SI Appendix*, Fig. S33*C* and Movie S3).

## Conclusions

The results presented here offer foundational guidelines associated with materials choices and designs for the integration of small-scale, hard device components into arrays that offer soft, biocompatible mechanics at the system level. The examples in energy harvesting, storage, and management represent some of the most important applications in biointegrated technologies. Other opportunities include chip-scale microelectromechanical technologies, radio devices, mechanical/thermal energy harvesting, and others. Further miniaturizing the dimensions of the associated components, deploying them in larger-scale arrays, and configuring the layouts to match geometrical and mechanical requirements associated with the anatomy at the point of biointegration are some interesting future directions for research.

## Materials and Methods

Details associated with the fabrication steps and the materials all appear in *SI Appendix*. The data acquisition system and related hardware for NFC data logging are shown in *SI Appendix*. Also, details of theoretical analysis are described in *SI Appendix*. The experiment for skin-mountable device was conducted at the University of Illinois at Urbana-Champaign (Institutional review board approved protocol: 15112).

**ACKNOWLEDGMENTS.** The authors used facilities in the Frederick Seitz Materials Research Laboratory at the University of Illinois at Urbana-Champaign. This work was supported by the Global Research Laboratory Program (K20704000003TA050000310) through the National Research Foundation of Korea funded by the Ministry of Science. Y.L. acknowledges support from National Basic Research Program of China Grant 2015CB351900. R.X. and Y.H. acknowledge support from NSF Grants DMR-1121262, CMMI-1300846, and CMMI-1400169 and the NIH Grant R01EB019337.

1. Xu S, et al. (2014) Soft microfluidic assemblies of sensors, circuits, and radios for the skin. *Science* 344(6179):70–74.
2. Axisa F, et al. (2007) Biomedical stretchable systems using mid based stretchable electronics technology. *Proceedings of the 29th Annual International Conference of the IEEE EMBS Cité Internationale* (IEEE, New York).
3. Someya T (2013) *Stretchable Electronics* (Wiley-VCH, Weinheim, Germany), pp 484.
4. Wagner S, Bauer S (2012) Materials for stretchable electronics. *MRS Bull* 37(3): 207–217.
5. Kim DH, et al. (2011) Epidermal electronics. *Science* 333(6044):838–843.
6. Kaltenbrunner M, et al. (2013) An ultra-lightweight design for imperceptible plastic electronics. *Nature* 499(7459):458–463.
7. Xu L, et al. (2014) 3D multifunctional integumentary membranes for spatiotemporal cardiac measurements and stimulation across the entire epicardium. *Nat Commun* 5:3329.
8. Kim DH, et al. (2010) Dissolvable films of silk fibroin for ultrathin conformal bio-integrated electronics. *Nat Mater* 9(6):511–517.
9. Song YM, et al. (2013) Digital cameras with designs inspired by the arthropod eye. *Nature* 497(7447):95–99.
10. Jang KI, et al. (2015) Soft network composite materials with deterministic and bio-inspired designs. *Nat Commun* 6:6566.
11. Hattori Y, et al. (2014) Multifunctional skin-like electronics for quantitative, clinical monitoring of cutaneous wound healing. *Adv Healthc Mater* 3(10):1597–1607.
12. Dagdeviren C, et al. (2015) Conformal piezoelectric systems for clinical and experimental characterization of soft tissue biomechanics. *Nat Mater* 14(7):728–736.
13. Jolly J (Jan. 10, 2016) 10 more great gadgets from CES 2016. *USA TODAY* www.usatoday.com/story/tech/columnist/2016/01/10/10-more-great-gadgets-ces-2016/78590554/. Accessed January 10, 2016.
14. Mei H, Irazoqui PP (2014) Miniaturizing wireless implants. *Nat Biotechnol* 32(10): 1008–1010.
15. Kim J, et al. (2015) Miniaturized flexible electronic systems with wireless power and near-field communication capabilities. *Adv Funct Mater* 25(30):4761–4767.
16. Kumar B, et al. (2011) Controlled growth of semiconducting nanowire, nanowall, and hybrid nanostructures on graphene for piezoelectric nanogenerators. *ACS Nano* 5(5): 4197–4204.
17. Wu W, et al. (2014) Piezoelectricity of single-atomic-layer MoS2 for energy conversion and piezotronics. *Nature* 514(7523):470–474.
18. Zhu G, Chen J, Zhang T, Jing Q, Wang ZL (2014) Radial-arrayed rotary electrification for high performance triboelectric generator. *Nat Commun* 5:3426.
19. Kim SJ, We JH, Cho BJ (2014) A wearable thermoelectric generator fabricated on a glass fabric. *Energy Environ Sci* 7(6):1959–1965.
20. Chan CK, et al. (2008) High-performance lithium battery anodes using silicon nanowires. *Nat Nanotechnol* 3(1):31–35.
21. Song T, et al. (2010) Arrays of sealed silicon nanotubes as anodes for lithium ion batteries. *Nano Lett* 10(5):1710–1716.
22. Hong J, et al. (2014) Biologically inspired pteridine redox centres for rechargeable batteries. *Nat Commun* 5:5335.
23. Jeong HM, et al. (2011) Nitrogen-doped graphene for high-performance ultracapacitors and the importance of nitrogen-doped sites at basal planes. *Nano Lett* 11(6):2472–2477.
24. Liu L, Yu Y, Yan C, Li K, Zheng Z (2015) Wearable energy-dense and power-dense supercapacitor yarns enabled by scalable graphene-metallic textile composite electrodes. *Nat Commun* 6:7260.
25. Jang KI, et al. (2014) Rugged and breathable forms of stretchable electronics with adherent composite substrates for transcutaneous monitoring. *Nat Commun* 5:4779.
26. Xu R, et al. (2014) Fabric-based stretchable electronics with mechanically optimized designs and prestrained composite substrates. *Extreme Mech Lett* 1:120–126.
27. Ko HC, et al. (2008) A hemispherical electronic eye camera based on compressible silicon optoelectronics. *Nature* 454(7205):748–753.
28. Su YW, et al. (2014) Mechanics of stretchable electronics on balloon catheter under extreme deformation. *Int J Solids Struct* 51(7-8):1555–1561.
29. Duc S, Arfaoui A, Polidori G, Bertucci W (2015) Efficiency and thermography in cycling during a graded exercise test. *J Exercise, Sports Orthop* 2(2):1–8.